A Novel Approach of Extracting Ship Scatterer's 3-DOF Micromotion Features Under Long Accumulation Time

Peng Zhou, *Member, IEEE*, Chuwen Cao, Yuru Li, Xi Zhang, Zhenhua Zhang, and Jie Zhang

***Abstract*—The rolling, pitching, and yawing motion of the vessel produces a micro-Doppler signature in the radar echoes. Ship scatterers' three-degree-of-freedom (3-DOF) micromotion features contain information on the ship geometric structure and motion parameters. Therefore, it is essential to extract the 3-DOF micromotion features of ship scatterers with high accuracy. Because existing approaches to extracting 3-DOF micromotion features of ship scatterers under long accumulation time have the disadvantage of low accuracy, we propose a high-precision algorithm based on linear micro-Doppler trajectory tracking after performing a generalized S-transform and ridge extraction to coarsely analyze the time-frequency trajectory corresponding to the ship's echo. To improve the extraction accuracy of 3-DOF micromotion features of ship scatterers, long time is divided into many short time segments. The motivation for time segmentation is that the instantaneous Doppler frequency of a scatterer caused by a ship's rotation is verified to behave approximately as a linear frequency modulation signal over a short period. The Doppler centroids and frequency modulation rates of scatterers during a short time segment in a given range bin can be easily coarsely estimated from ridge extraction results. The instantaneous Doppler frequency trajectories of the same scatterer in adjacent short time segments are correlated and filtered by using the nearest neighbor algorithm and the extended Kalman filtering algorithm to achieve high estimation accuracy. The results of the performed simulation and processing of real radar data verify the accuracy of the proposed algorithm is higher than those of the current commonly used algorithms.**

***Index Terms*—Linear micro-Doppler trajectory tracking, long accumulation time, three-degree-of-freedom (3-DOF) micromotion feature, time segmentation.**

Manuscript received 11 July 2022; revised 5 September 2022; accepted 23 September 2022. Date of publication 28 September 2022; date of current version 7 October 2022. This work was supported in part by the Shandong Provincial Natural Science Foundation under Project ZR2019MF004, in part by the Key Funds of National Natural Science Foundation of China under Grant 61931025, and in part by the National Natural Science Foundation of China under Grant 61971455. *(Corresponding author: Peng Zhou.)*

Peng Zhou, Chuwen Cao, and Yuru Li are with the College of Oceanography and Space Informatics, China University of Petroleum, Qingdao 266580, China (e-mail: zhoupeng@upc.edu.cn; s20160027@s.upc.edu.cn; liyuru4@sina.com).

Xi Zhang is with the First Institute of Oceanography, Ministry of Natural Resources of the People's Republic of China, Qingdao 266061, China (e-mail: xi.zhang@fio.org.cn).

Zhenhua Zhang is with the Beijing Research Institute of Telemetry, Beijing 100076, China (e-mail: 13522625991@163.com).

Jie Zhang is with the College of Oceanography and Space Informatics, China University of Petroleum, Qingdao 266580, China, and also with the First Institute of Oceanography, Ministry of Natural Resources of the People's Republic of China, Qingdao 266061, China (e-mail: zhangjie@fio.org.cn).

Digital Object Identifier 10.1109/JSTARS.2022.3210048

I. Introduction

THE classification and recognition of ships sailing on the sea have important application value in both military and civil fields [1]. Currently, the main way for radar to recognize ships is to use high-resolution synthetic aperture radar (SAR) or inverse synthetic aperture radar (ISAR) images [2]. However, due to waves and other factors, ships moving on the sea nonuniformly rotate in three axes, roll, pitch, and yaw. This makes the magnitude and direction of the synthesized rotation vector always change with time, which seriously affects the quality of ship subimages in SAR and ISAR images [3]. The 3-D rotations of a ship are the direct cause of poor radar image quality. On the other hand, the micromotion characteristics caused by the rotations of the ship in three degrees of freedom (3-DOF) contain the geometric structure and motion parameter information of the ship. For clarity, in this article, we define the 3-DOF micromotion feature as the micro-Doppler frequency variation of the scatterer caused only by the 3-DOF rotations of the ship when the radar is stationary and the translational speed of the ship is zero or the translational movements of the radar and the ship are compensated. Clearly, it is important to extract the 3-DOF micromotion features of ship scatterers with high accuracy to improve the imaging quality of ships and realize the 3-D imaging of ships [4], [5]. With the improvement of SAR image quality, the detection probability of ship detection system will be improved under the condition that the false alarm rate is constant [6], [7]. The ability of 3-D imaging of ships will greatly improve the accuracy of ship classification, because 3-D structure of a ship is a feature with strong robustness for the classification [8], [9].

In recent years, the technology related to the extraction of micromotion features has become a research highlight to meet the needs of ship detection, imaging, and recognition. At present, there are several types of algorithms to extract the micromotion characteristics of scatterers in a target, such as time-frequency analysis, image processing, sinusoidal frequency modulation Fourier transform, and linear frequency modulation estimation of sparse multicomponent [10]. Time-frequency analysis-based algorithms can be divided into linear transformation and nonlinear transformation. Linear transforms include the short-time Fourier transform (STFT) [11], [12], wavelet transform [13], S-transform [14], etc. Nonlinear transforms include the Wigner–Ville distribution (WVD) [15], smoothed pseudo Wigner–Ville

distribution (SPWVD) [16], etc. Ding et al. extracted the instantaneous Doppler frequency of the human calf using the STFT algorithm and synthesized the target trajectory through Doppler frequency processing [17]. Suresh et al. decomposed a nonstationary signal based on an algorithm combining the WVD and fractional-order Fourier transform and employed the WVD to estimate the instantaneous Doppler frequencies of individual components, avoiding the problem of cross-term interference when only the WVD is used to analyze multicomponent signals [18]. It should be noted that although time-frequency analysis methods can reveal the time-frequency characteristics contained in the signal in the time-frequency plane, there is often cross-term interference using nonlinear transformations to analyze multicomponent signals. Moreover, linear transforms have the disadvantage that the time-frequency resolution adjustment ability is relatively weak [19]. Image-processing-based methods first obtain the time-frequency distribution (TFD) using tools, such as time-frequency analysis. Then, the instantaneous Doppler frequency is obtained by extracting the given shape on the TFD map using tools, such as the Hough transform and generalized Radon transform. Fang et al. considered the micro-Doppler feature extraction of small unmanned rotorcraft (SUR). The Gabor transform is utilized to obtain the TFD, and the Hough–Radon transform (HRT) is introduced to detect the sinusoidal curves from the TFD. Finally, based on the relationship between the sinusoidal curves and the rotating blade, the micro-Doppler parameters, such as the rotation frequencies of the SUR's blades are estimated [20]. It should be noted that this type of algorithm is based on the assumption that the radar echo satisfies an established signal model. If the parametric model established cannot be guaranteed to match the radar echo, this type of algorithm is no longer applicable. In addition, the computational load of this type of algorithm increases exponentially, and the accuracy of the estimation results decreases with increasing dimensionality of the parameter space. Methods based on the sinusoidal frequency modulation Fourier transform take advantage of the characteristic that micro-Doppler signals caused by micromotions, such as rotations behave as sinusoidal frequency modulation signals. They use the sinusoidal frequency modulation Fourier transform and other tools to estimate scatterers' instantaneous Doppler frequency history [21]. For example, Peng et al. used an algorithm based on the sinusoidal frequency modulation Fourier transform to calculate the spectrum induced by a target's vibration and solve problems, such as phase unwrapping for the purpose of extracting micromotion features with high accuracy [22]. However, when there are more than three components, algorithms based on the sinusoidal frequency modulation Fourier transform suffers from cross-term interference, making it difficult to separate the signal components accurately. Methods based on the linear frequency modulation estimation of sparse multicomponent can estimate an unknown number of uncorrelated multiple linear frequency components and have strong robustness to noise. Zhou et al. proposed an estimation algorithm combining data extrapolation with compressed sensing, making use of the property that the instantaneous Doppler frequency of a scatterer on a ship exhibits a linear frequency modulation signal in a short time segment [23]. The computation load of methods based on the linear frequency modulation estimation of sparse multicomponent is relatively large because the processing includes sparse reconstruction iteration. It should be noted that when estimating the instantaneous Doppler frequency in the case of a long accumulation time, the estimation accuracy of this type of method needs to be improved because the instantaneous Doppler frequency variation of a ship scatterer is nonlinear. The above research status shows that an algorithm to extract the 3-DOF micromotion characteristics of ship scatterers with high accuracy under long accumulation time is still difficult to solve.

In this article, an algorithm based on linear micro-Doppler trajectory tracking is proposed to achieve high-precision extraction of 3-DOF micromotion features under a long accumulation time. First, a generalized S-transform algorithm is used to obtain the TFD, and the ridges of scatterers on a ship are extracted by an algorithm featured using energy functional minimization. Next, according to the characteristics that a scatterer's instantaneous Doppler frequency caused by the ship's three-axis rotation is a linear frequency modulation signal in a short time, the long accumulation time is segmented to estimate the Doppler centroid frequency and the frequency rate in each short time segment. Then, based on the idea of approximating the curve as a broken line composed of multiple short line segments, the correlation and filtering of the instantaneous Doppler frequency trajectories of the same scatterer in adjacent short time segments are completed using the nearest neighbor association, Kalman filtering and other related algorithms. Finally, the high-precision extraction of the instantaneous Doppler frequency over a long accumulation time is realized after the above processing steps are completed. The characteristic of the proposed algorithm is using a broken line to approximate a curve, without the need to deduce the accurate analytical expression of the instantaneous Doppler frequency under a long accumulation time. The effectiveness of the proposed algorithm is verified by comparing the extraction accuracy of the proposed algorithm with those of existing algorithms using both simulation and experiments performed on a turntable.

The rest of this article is organized as follows. Section II introduces the geometry model and analyzes the characteristics of the 3-DOF micromotion characteristics of a ship scatterer under a long accumulation time. Section III presents the proposed algorithm to extract the 3-DOF micromotion feature based on linear micro-Doppler trajectory tracking in detail and summarizes the processing flow of the proposed algorithm. The simulation and real data processing results are presented in Section IV. In this section, the extraction accuracies of the proposed algorithm, an algorithm combining a generalized S-transform with ridge extraction, and the algorithm in [23] under a long accumulation time are compared to verify the higher accuracy of the proposed algorithm. Finally, Section V concludes this article.

II. Geometry Model and Analysis of 3-DOF Micromotion Features Under a Long Accumulation Time

A. Geometry Model

In this article, the 3-DOF micromotion feature refers to the instantaneous Doppler frequency of a scatterer caused by the 3-DOF rotations of the ship when the radar is stationary and

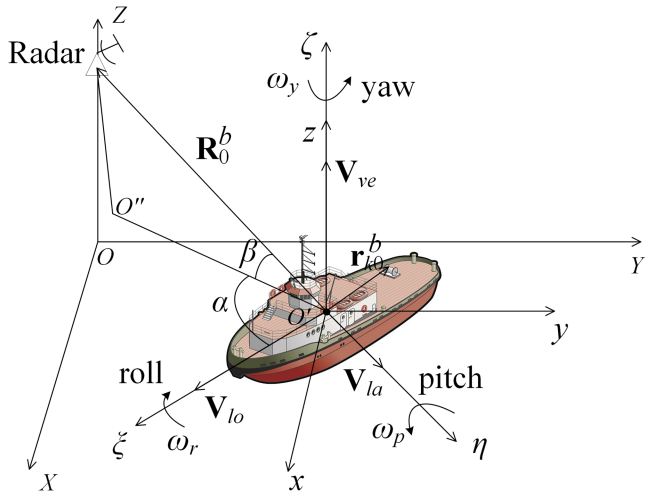

Fig. 1. Geometry model of the system.

the vessel has no translational component. Therefore, it is assumed that the motion of the radar platform and the translation component of the ship have been compensated by a translation compensation algorithm.

The geometry model of the system is shown in Fig. 1. The coordinate system XYZ is the radar coordinate system E_r, and the origin o is the projection of the radar on the ground plane at the imaging center moment. The *X*-axis points to the local geographical north, the *Y*-axis points to the local geographical west, and the *Z*-axis points vertically upward. The coordinate system xyz is the ship reference coordinate system E_f, whose axes are defined in the same way as those of the coordinate system XYZ, except with the origin o' being the rotation center of the ship. The coordinate system $\xi\eta\zeta$ is the ship's body coordinate system E_b at the central moment, where the ξ axis points in the bow direction at the imaging central moment, the η axis points in the port side direction of the ship at the central moment of imaging, and the pointing of the ζ axis is determined by the right-hand rule. For sake of simplicity, it is assumed that the change between E_b and E_f is given by only a rotation around z-axis, so that the direction of ζ axis coincides with that of z-axis. ω_r, ω_p, and ω_y represent the angular velocities of the ship's rotations in the roll, pitch, and yaw axes, respectively. $\mathbf{V}_{lo}$, $\mathbf{V}_{la}$, and $\mathbf{V}_{ve}$ are vectors corresponding to the longitudinal speed, lateral speed, and vertical speed of the ship, respectively. Note that these speed components of the ship are assumed to have been compensated. $\mathbf{R}_0^b$ denotes the position vector from the rotation center of the ship to the radar defined in the coordinate system E_b, and $\mathbf{r}_{k0}^b$ is the position vector of the *k*th scatterer at the imaging center moment. o'' is the projection of the radar in the $\xi o'\eta$ plane, α is the angle between line $o'o''$ and the ξ axis, and β is the angle between lines $o'o''$ and $\mathbf{R}_0^b$.

For a scatterer on the ship in Fig. 1, the 3-DOF rotations of the ship cause a rotational motion of the scatterer relative to the ship's rotation center which results in a continuous change in the instantaneous Doppler frequency of the scatterer. The rotation matrices of the ship corresponding to the yaw, roll, and pitch can be expressed as [24], [25], [26]

$$\text{Yaw}\left(\theta_y\left(t\right)\right) = \begin{bmatrix} \cos\theta_y\left(t\right) & -\sin\theta_y\left(t\right) & 0 \\ \sin\theta_y\left(t\right) & \sin\theta_y\left(t\right) & 0 \\ 0 & 0 & 1 \end{bmatrix} \tag{1}$$

$$\text{Roll}\left(\theta_r\left(t\right)\right) = \begin{bmatrix} 1 & 0 & 0 \\ 0 & \cos\theta_r\left(t\right) & -\sin\theta_r\left(t\right) \\ 0 & \sin\theta_r\left(t\right) & \cos\theta_r\left(t\right) \end{bmatrix} \tag{2}$$

$$\text{Pitch}\left(\theta_p\left(t\right)\right) = \begin{bmatrix} \cos\theta_p\left(t\right) & 0 & \sin\theta_p\left(t\right) \\ 0 & 1 & 0 \\ -\sin\theta_p\left(t\right) & 0 & \cos\theta_p\left(t\right) \end{bmatrix} \tag{3}$$

where $\theta_y(t)$, $\theta_p(t)$, and $\theta_r(t)$ represent the rotation angles corresponding to the yaw, pitch, and roll at time t, respectively.

The composite rotation matrix of the ship can be expressed as (4) shown at the bottom of the next page.

At the central moment of imaging, if the coordinate of scatterer *k* on the ship in E_b is $[\xi_{k0}, \eta_{k0}, \zeta_{k0}]$, then at any time t, the coordinate of scatterer k on the ship in E_b is

$$\left[\xi_k\left(t\right), \eta_k\left(t\right), \zeta_k\left(t\right)\right]^T = \begin{bmatrix} a_{11} & a_{12} & a_{13} \\ a_{21} & a_{22} & a_{23} \\ a_{31} & a_{32} & a_{33} \end{bmatrix} \cdot \left[\xi_{k0}, \eta_{k0}, \zeta_{k0}\right]^T. \tag{5}$$

Additionally, the coordinates of scatterer k on the ship in E_f can be expressed as

$$\begin{bmatrix} b_{11} & b_{12} & b_{13} \\ b_{21} & b_{22} & b_{23} \\ b_{31} & b_{32} & b_{33} \end{bmatrix} \cdot \left[\xi_k\left(t\right), \eta_k\left(t\right), \zeta_k\left(t\right)\right]^T \tag{6}$$

where (7) shown at the bottom of the next page, where θ_{y0}, θ_{p0}, and θ_{r0} are the yaw, pitch, and roll angles corresponding to the rotation from the E_b coordinate system to the E_f coordinate system, respectively.

At any time t, the instantaneous distance between the radar and scatterer k on the ship is [27]

$$R_k\left(t\right) = \left| \left[X_0, Y_0, Z_0\right]^T + \begin{bmatrix} b_{11} & b_{12} & b_{13} \\ b_{21} & b_{22} & b_{23} \\ b_{31} & b_{32} & b_{33} \end{bmatrix} \cdot \begin{bmatrix} a_{11} & a_{12} & a_{13} \\ a_{21} & a_{22} & a_{23} \\ a_{31} & a_{32} & a_{33} \end{bmatrix} \cdot \left[\xi_{k0}, \eta_{k0}, \zeta_{k0}\right]^T - \left[0,0,H\right]^T \right| \tag{8}$$

where H is the height of the radar platform and $[X_0, Y_0, Z_0]$ are the coordinates of the ship's rotation center in the radar coordinate system E_r at the imaging center moment. Clearly, the instantaneous Doppler frequency of scatterer k is

$$f_{dk}\left(t\right) = -\frac{2}{\lambda}\frac{dR_k\left(t\right)}{dt} \tag{9}$$

where λ is the wavelength. When the accumulation time is relatively short, the analytical expression for the instantaneous

Doppler frequency of scatterer k can be approximated as [23]

$$f_{dk}(t) \approx \frac{2}{\lambda} \cdot \begin{bmatrix} (\eta_{k0} m_3 - \zeta_{k0} m_2) \cdot A_r \cdot \cos\left(\frac{2\pi}{T_r} t + \phi_r\right) + \\ (\zeta_{k0} m_1 - \xi_{k0} m_3) \cdot A_p \cdot \cos\left(\frac{2\pi}{T_p} t + \phi_p\right) + \\ (\xi_{k0} m_2 - \eta_{k0} m_1) \cdot A_y \cdot \cos\left(\frac{2\pi}{T_y} t + \phi_y\right) \end{bmatrix} \tag{10}$$

where m_1, m_2, and m_3 are the 3-D coordinates of the unit vector corresponding to $\mathbf{R}_0^b$. A_r, T_r, and ϕ_r are the amplitude, period, and initial phase of the cosine angular velocity of the roll, A_p, T_p, and ϕ_p are the amplitude, period, and initial phase of the cosine angular velocity of the pitch, and A_y, T_y, and ϕ_y are the amplitude, period, and initial phase of the cosine angular velocity of the yaw, respectively.

B. Analysis of 3-DOF Micromotion Feature of Ship Scatterers Under a Long Accumulation Time

It should be noted that (10) holds only when the accumulation time is relatively short. When the accumulation time is longer, the error of the instantaneous Doppler frequency of a scatterer calculated using (10) is larger. To quantitatively illustrate the magnitude of the error, some typical data [28], as shown in Table I, are used for calculation. The truth value of the instantaneous Doppler frequency of each scatterer was achieved by calculating the change in the instantaneous distance between the radar and the scatterer by (9). The model value of the instantaneous Doppler frequency of the scatterer was calculated by (10).

Fig. 2 compares the model value with the true value of the instantaneous Doppler frequency of a scatterer. Fig. 2(a) and (b) show the cases in which the synthetic aperture times are 1 and 10 s, respectively. The accuracy of the model value is higher in Fig. 2(a), while the error of the model value is relatively large in Fig. 2(b). According to statistics, the mean square error corresponding to Fig. 2(a) is only approximately 0.4 Hz, whereas the mean square error corresponding to Fig. 2(b) reaches approximately 5.2 Hz. It is obvious that the accuracy of the existing micro-Doppler model is relatively low in the case of a long accumulation time, so it is necessary to study the 3-DOF micromotion feature extraction algorithm that does not depend on a micro-Doppler model.

Previous studies have shown that the instantaneous Doppler frequency of a scatterer approximately obeys a linear frequency

TABLE I
TYPICAL DATA FOR ANALYZING THE 3-DOF MICROMOTION FEATURES OF SHIP SCATTERERS

Parameter	Value	Parameter	Value
Radar platform speed	0 m/s	Synthetic aperture time	1 s, 10 s
Ship translation speed	0 m/s	Platform altitude	5 km
Carrier frequency	5.4 GHz	α	0°
Amplitude of angular velocity in the roll	0.1726 rad/s	β	20°
Period of angular velocity in the roll	12.2 s	Initial phase of angular velocity in the roll	330°
Amplitude of angular velocity in the pitch	0.0278 rad/s	Period of angular velocity in the pitch	6.7 s
Initial phase of angular velocity in the pitch	284°	Amplitude of angular velocity in the yaw	0.0147 rad/s
Period of angular velocity in the yaw	14.2 s	Initial phase of angular velocity in the yaw	105°
Scatterer's coordinate in $\xi\eta\zeta$ coordinate system	(100,0,0)	Coordinates of O' in XYZ coordinate system	(0,13737.4,0)

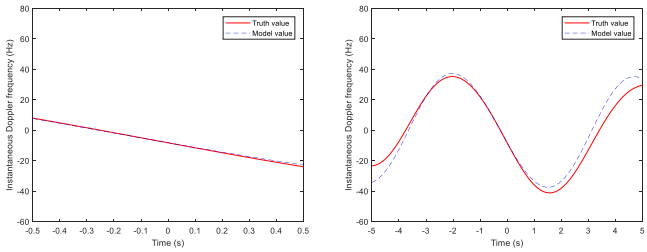

Fig. 2. Comparison of model and truth values of the instantaneous Doppler frequency of a scatterer. (a) Synthetic aperture time is 1 s. (b) Synthetic aperture time is 10 s.

$$\begin{aligned} \mathrm{Rot}\left[\theta_r(t), \theta_p(t), \theta_y(t)\right] &= \mathrm{Roll}\left[\theta_r(t)\right] \cdot \mathrm{Pitch}\left[\theta_p(t)\right] \cdot \mathrm{Yaw}\left[\theta_y(t)\right] \\ &= \begin{bmatrix} a_{11} & a_{12} & a_{13} \\ a_{21} & a_{22} & a_{23} \\ a_{31} & a_{32} & a_{33} \end{bmatrix} \\ &= \begin{bmatrix} \cos\theta_p(t)\cos\theta_y(t) & -\cos\theta_p(t)\sin\theta_y(t) & \sin\theta_p(t) \\ \sin\theta_r(t)\sin\theta_p(t)\cos\theta_y(t) & -\sin\theta_r(t)\sin\theta_p(t)\sin\theta_y(t) & -\sin\theta_r(t)\cos\theta_p(t) \\ +\cos\theta_r(t)\sin\theta_y(t) & +\cos\theta_r(t)\cos\theta_y(t) & \\ -\cos\theta_r(t)\sin\theta_p(t)\cos\theta_y(t) & \cos\theta_r(t)\sin\theta_p(t)\sin\theta_y(t) & \cos\theta_r(t)\cos\theta_p(t) \\ +\sin\theta_r(t)\sin\theta_y(t) & +\sin\theta_r(t)\cos\theta_y(t) & \end{bmatrix}. \end{aligned} \tag{4}$$

$$\begin{bmatrix} b_{11} & b_{12} & b_{13} \\ b_{21} & b_{22} & b_{23} \\ b_{31} & b_{32} & b_{33} \end{bmatrix} = \begin{bmatrix} \cos\theta_{p0}\cos\theta_{y0} & -\cos\theta_{p0}\sin\theta_{y0} & \sin\theta_{p0} \\ \sin\theta_{r0}\sin\theta_{p0}\cos\theta_{y0} & -\sin\theta_{r0}\sin\theta_{p0}\sin\theta_{y0} & -\sin\theta_{r0}\cos\theta_{p0} \\ +\cos\theta_{r0}\sin\theta_{y0} & +\cos\theta_{r0}\cos\theta_{y0} & \\ -\cos\theta_{r0}\sin\theta_{p0}\cos\theta_{y0} & \cos\theta_{r0}\sin\theta_{p0}\sin\theta_{y0} & \cos\theta_{r0}\cos\theta_{p0} \\ +\sin\theta_{r0}\sin\theta_{y0} & +\sin\theta_{r0}\cos\theta_{y0} & \end{bmatrix} \tag{7}$$

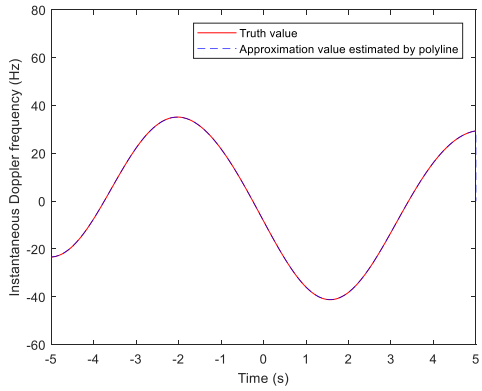

Fig. 3. True value curve of the instantaneous Doppler frequency and the broken line formed by connecting the lines corresponding to each short time segment.

modulation law in a relatively short time segment. According to the principle that the second-order term of the Taylor expansion of the instantaneous Doppler frequency does not exceed half of the Doppler resolution, the formula for the appropriate length of the short time segment is obtained as [23]

$$T_{\text{seg}} \le \sqrt{\frac{\rho_f/\pi^2}{\left[\frac{|A'_{rk}|}{T_r^2}+\frac{|A'_{pk}|}{T_p^2}+\frac{|A'_{yk}|}{T_y^2}\right]_{\max}}}, 1 \le k \le K \quad (11)$$

where T_{seg} is the length of the short time segment, ρ_f is the Doppler resolution, K is the number of scatterers, and there is [23]

$$\begin{aligned} A'_{rk} &= \frac{2}{\lambda}\cdot(\eta_{k0}m_3-\zeta_{k0}m_2)\cdot A_r \\ A'_{pk} &= \frac{2}{\lambda}\cdot(\zeta_{k0}m_1-\xi_{k0}m_3)\cdot A_p \\ A'_{yk} &= \frac{2}{\lambda}\cdot(\xi_{k0}m_2-\eta_{k0}m_1)\cdot A_y. \end{aligned} \quad (12)$$

The physical meaning of (11) is clear. However, it is not convenient to use (11) to estimate the length of a short time segment because the rotation parameters of the ship are usually unknown. In fact, empirically, it is appropriate to take the value of T_{seg} as no more than 0.1 s. To verify the above conclusion the value of T_{seg} was set to 0.1 s. Then, the truth value curve of the instantaneous Doppler frequency in Fig. 2(b) was divided into segments of length 0.1 s, and the starting and the ending frequencies of each segment were connected to form a broken line. Fig. 3 shows the truth value curve of the instantaneous Doppler frequency and the broken line formed by connecting the lines corresponding to each short time segment. It can be seen from the figure that the true value curve and broken line are very close to each other. Statistically, the mean square error between the true value curve and broken line is only 0.03 Hz. Therefore, the instantaneous Doppler frequency curve can be estimated with high precision by estimating the Doppler centroid frequency and the frequency rate for each short time segment. It is unnecessary to deduce the accurate analytical expression of the instantaneous Doppler frequency under a long accumulation time using the above algorithm to estimate the 3-DOF micromotion characteristics of the ship scatterer.

III. 3-DOF Micromotion Feature Extraction Approach Applicable to Long Accumulation

A. Echo Model

The echo signal of a ship in the azimuth time-range frequency domain is [23]

$$\begin{aligned} s'(t,f_r) = W(t,f_r)\cdot e^{-j\frac{4\pi}{C}f_r R_0(t)}\cdot \int A(\mathbf{r},t) \\ \cdot \sigma_0(\mathbf{r})\cdot e^{-j\frac{4\pi}{C}f_r\left[\mathbf{r}^T\cdot \mathbf{i}_{\mathbf{R_0}}(t)\right]}d\mathbf{r} \end{aligned} \quad (13)$$

where t is the azimuth time, f_r is the range frequency, $W(t,f_r)=\text{rect}\left(\frac{t}{T_{\text{int}}}\right)\cdot\text{rect}\left(\frac{f_r-f_c}{B}\right)$, rect$(\cdot)$ is a rectangular function, T_{int} is the accumulation time, f_c is the carrier frequency, B is the bandwidth, and C is the speed of light. $\mathbf{R_0}(t)$ represents the time-varying vector from the radar phase center to the ship's rotation center, $R_0(t)$ represents the modulus of $\mathbf{R_0}(t)$, $\boldsymbol{i}_{\mathbf{R_0}}(t)$ is the unit vector of $\mathbf{R_0}(t)$, $\mathbf{r}$ is the vector from the ship's rotation center to a scatterer on the ship, and $\sigma_0(\mathbf{r})$ is the normalized radar cross section (RCS) of scatterer located at $\mathbf{r}$. $A(\mathbf{r},t)$ consists of the transmitted signal power, the distance between the radar and ship, the antenna pattern both in the range and azimuth directions, and other factors that affect the amplitude and phase of the echo.

After range compression, envelope alignment and translational phase compensation are performed, the echo signal can be expressed as [23]

$$\begin{aligned} s(t,\tau) = \text{rect}\left(\frac{t}{T_{\text{int}}}\right)\cdot\sum_{k=1}^{K_{\text{total}}}\{A_k(t)\cdot\sigma_k\cdot B \\ \cdot \text{sinc}\left[B(\tau-\tau_k)\right] \\ \cdot e^{-j2\pi f_c\tau_k}e^{j2\pi\int f_{dk}(t)dt}\} \end{aligned} \quad (14)$$

where τ is the range time, k is the index of a scatterer, K_{total} is the total number of scatterers, $A_k(t)$ is the $A(\mathbf{r},t)$ corresponding to scatterer k, σ_k is the RCS of scatterer k, τ_k is the shortest two-way delay time corresponding to scatterer k, and $f_{dk}(t)$ is the instantaneous micro-Doppler frequency of scatterer k.

Let l represent the index of a range bin; then, the azimuth echo of the lth range bin can be expressed as

$$\begin{aligned} s_l(t) = \text{rect}\left(\frac{t}{T_{int}}\right)\cdot\sum_{k=1}^{K}\{A_k(t)\cdot\sigma_k\cdot B \\ \cdot \text{sinc}\left[B(\tau_l-\tau_k)\right]\cdot e^{-j2\pi f_c\tau_k}e^{j2\pi\int f_{dk}(t)dt}\} \end{aligned} \quad (15)$$

where K is the number of scatterers contained in the lth range bin, and τ_l is the two-way delay time corresponding to the lth range bin. The task of the algorithm to extract the 3-DOF micromotion features is first to identify the range bins containing the scatterers of the ship and then to extract the instantaneous micro-Doppler frequencies of each scatterer in the identified range bins.

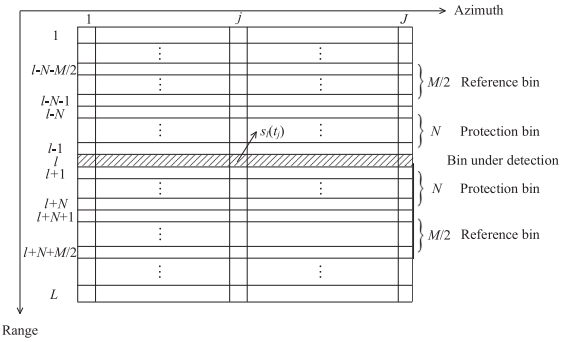

Fig. 4. Meanings of the relevant symbols in the detection of range bins containing ship scatterers.

B. Detection of Range Bins Containing Ship Scatterers

To identify range bins containing scatterers, the problem can be transformed into a signal detection operation with a constant false alarm rate. The main related formulas are

$$\hat{\mu}_{cl} = \frac{1}{M} \cdot \left[\sum_{i=l-N-\frac{M}{2}}^{l-N-1} A_i + \sum_{i=l+N+1}^{i=l+N+\frac{M}{2}} A_i \right] \tag{16}$$

$$\hat{\sigma}_{cl} = \sqrt{\frac{1}{M-1} \left[\sum_{i=l-N-\frac{M}{2}}^{l-N-1} (A_i - \hat{\mu}_{cl})^2 + \sum_{i=l+N+1}^{i=l+N+\frac{M}{2}} (A_i - \hat{\mu}_{cl})^2 \right]} \tag{17}$$

$$A_i = \sqrt{\sum_{j=1}^{J} |s_i(t_j)|^2}, 1 \le i \le I \tag{18}$$

$$\frac{A_l - \hat{\mu}_{cl}}{\hat{\sigma}_{cl}} \underset{H_0}{\overset{H_1}{\gtrless}} K_{\text{CFAR}} \tag{19}$$

where N represents the number of protection bins on one side of the bin to be detected, and M represents the number of reference bins on both sides of the bin to be detected. $\hat{\mu}_{cl}$ and $\hat{\sigma}_{cl}$ represent the mean and the standard deviation of the amplitude of the reference bins corresponding to the *l*th range bin, respectively. A_l represents the average amplitude of the *l*th range bin, L is the number of all range bins, t_j is the azimuth time corresponding to the *j*th azimuth sampling bin, *J* is the number of all azimuth sampling bins, $s_l(t_j)$ is the signal corresponding to the *l*th range bin in the *j*th azimuth sampling bin, H_1 and H_0 represent the hypotheses that the current range bin contains and does not contain ship scatterers, respectively, and K_{CFAR} is a constant associated with the expected false alarm rate. The meanings of the above relevant symbols is illustrated in Fig. 4. As displayed in Fig. 4, protection bins are reserved on each side of the bin under detection to avoid leakage of signal components since a ship may occupy several bins. The total number of a half of protection bins is set to be slightly larger than the number of bins corresponding to the maximum ship to be detected. The average and the standard deviation of the amplitudes of reference bins are calculated to judge whether the bin under detection contains ship scatterer according to (19), where K_{CFAR} is determined by the expected false alarm rate.

C. Rough Time-Frequency Trajectory Estimation of Ship Scatterers Based on Generalized S-Transform Combined With Ridge Extraction

The ideal time-frequency analysis method should not only enable the echo signal to obtain a higher time-frequency concentration but also accurately reflect the instantaneous Doppler frequency of the linear frequency modulation signal. Time-frequency analysis methods based on nonlinear transformation are often limited to the problem of multicomponent cross-term interference. In contrast, the relatively weak adjustment ability of time-frequency resolution often limits the application of methods classified as linear transformation. An S-transform is a linear transform type of time-frequency analysis method that has been widely used in recent years. Its main advantage is that it has the advantages of both short-time Fourier transform and wavelet transform, except that there is no cross interference of multiple components. An S-transform exploits both a varying window function and a Fourier transform kernel and introduces a Gaussian window function whose width varies inversely with the frequency while maintaining the signal phase information. Thus, it has variable time-frequency resolution [29]. An S-transform overcomes the drawback of fixed time-frequency resolution of the short-time Fourier transform and solves the disadvantages, such as phase localization in wavelet transform. Similar to multiresolution analysis methods, such as a wavelet transform, an S-transform has a higher frequency resolution at low frequencies and a higher time resolution at high frequencies.

In practical applications, it sometimes also needs high-frequency resolution at high frequency. A traditional S-transform is limited in such applications because the standard deviation of the Gaussian window function is fixed as the reciprocal of the frequency, which cannot satisfy the above demand. In other words, the adjustment ability of the time-frequency resolution with regard to a traditional S-transform is not strong. A generalized S-transform can improve the time-frequency resolution adjustment ability by setting parameters that can adjust the width of the Gaussian window [30]. Therefore, with regard to a range bin that is detected as containing scatterers of a ship and whose index is l, a generalized S-transform is performed to estimate the time-frequency trajectories of several scatterers in the range bin. The specific formula for the generalized S-transform is

$$\text{GST}(t, f_d; \gamma, q) = \int_{-\infty}^{\infty} s_l(\tau) w(t - \tau, f_d, \gamma, q) e^{-j2\pi f_d \tau} d\tau \tag{20}$$

where $s_l(\tau)$ is the signal of the *l*th range bin after range compression, envelope alignment, and translational phase compensation, $\text{GST}(t, f_d; \gamma, q)$ denotes the signal after the operation on $s_l(\tau)$ using the generalized S-transform, f_d is the Doppler frequency, γ and q are the two parameters to adjust the width of the Gaussian window, and w is the Gaussian window function. The Gaussian window function w is defined as

$$w(\tau, f_d, \gamma, q) = \frac{\gamma |f_d|^q}{\sqrt{2\pi}} e^{-\frac{\tau^2}{2} \gamma^2 f_d^{2q}}. \tag{21}$$

The standard deviation in the Gaussian function corresponding to (21) is

$$\sigma(f_d) = \frac{1}{\gamma |f_d|^q}. \tag{22}$$

When both values of γ and q in (22) are set to 1, the generalized S-transform transforms to a standard S-transform, and the denominator of the standard deviation in such cases varies linearly with the Doppler frequency. When the value of q is less than 1, the denominator of the standard deviation shows a nonlinear variation in the form of a convex function. When the value of q is greater than 1, the denominator of the standard deviation shows a nonlinear variation in the form of a concave function. When q is determined, the regulating factor γ can be adjusted to increase or decrease the curvature to strengthen the regulatory effect induced by q. It can be verified that the time resolution Δt and frequency resolution Δf corresponding to the above generalized S-transform are

$$\Delta t = \frac{1}{\sqrt{2}\gamma f_d^q} \tag{23}$$

$$\Delta f = \frac{\gamma f_d^q}{2\sqrt{2}\pi}. \tag{24}$$

When $\gamma < 1$ or $q < 1$, compared with the traditional S-transform, the frequency resolution of the spectrum corresponding to the generalized S-transform is improved. When $\gamma > 1$ or $q > 1$, compared with the traditional S-transform, the time resolution of the spectrum corresponding to the generalized S-transform is improved. It can be seen that the generalized S-transform improves the adjustment ability of the time-frequency resolution by supplementing the adjustment parameters of the Gaussian window function.

For the range bin containing ship scatterers and whose index is l, a ridge extraction algorithm is employed on the time-frequency analysis results obtained by the generalized S-transform. In this article, an algorithm featuring energy functional minimization is used for ridge extraction. This algorithm adds a penalty function to the TFD results and extracts the time-frequency ridge with the maximum energy while ensuring a smooth curve. The core formula of the algorithm featured using energy functional minimization [31], [32], [33] is (25) shown at the bottom of this page, where GST represents the TFD of the signal achieved by the generalized S-transform, k represents the ridge index, K represents the number of ridges, $\hat{f}_{d,k}(t)$ denotes the instantaneous Doppler frequency that corresponds to the kth ridge at time t, and μ_1 and μ_2 are two parameters to adjust the regularization level. μ_1 and μ_2 are used to balance the smoothness and the energy of the curve corresponding to the time-frequency analysis results. It should be noted that the first term has a negative sign in the summation sign of (25), so the essence of the minimization of (25) is to find multiple smooth curves with maximum energy.

D. Linear Micro-Doppler Trajectory Tracking

Although the time-frequency ridges of multiple scatterers corresponding to a certain range bin can be obtained by the ridge extraction algorithm, the accuracy of the estimation results still needs to be improved, especially in the vicinity of the intersections of multiple trajectories, where relatively large errors may occur.

The proposed algorithm is based on the characteristic that the micro-Doppler frequency changes approximately linearly in a short time segment. The whole accumulation time is divided into many short time segments. The estimated values of the Doppler centroid frequency and Doppler frequency rate are obtained using the results after ridge extraction in each time segment, and then the multitarget tracking algorithm is used to track the scatterers of a ship. The estimated values of the Doppler centroid frequency and Doppler frequency rate obtained by the ridge extraction algorithm are considered radar measurements. The Doppler centroid frequency and Doppler frequency rate of the previous time segment are used to predict the Doppler centroid frequency and Doppler frequency rate of the next time segment. The extended Kalman filtering technique is then used to filter the measurement and the prediction to improve the estimation accuracy. The Kalman filtering can be used to obtain dynamic estimates of the target in the linear Gaussian case using the mean square error criterion. However, in practice the relationship between the observed data and the dynamic parameters of the target is nonlinear, and the nonlinear filtering problem needs to be transformed into an approximately linear filtering problem using linearization methods. Accordingly this article uses the extended Kalman filtering method [34], [35]. The above processing makes full use of the characteristic that the Doppler centroid frequency of adjacent time segments does not change greatly and can correct the large errors in the ridge extraction results near the intersection of multiple time-frequency trajectories. Finally, the instantaneous Doppler frequency of each scatterer can be extracted with high accuracy.

Multitarget tracking techniques for radars mainly include track initiation algorithms, data association algorithms, and filtering algorithms [36]. Track initiation is the first step in multitarget tracking processing, and a logic-based algorithm to track initiation [37] is chosen in this article. First, the radar measurement points in the initial time segment are taken as the start of the track, and an initial correlation gate is established. Possible tracks are established for the radar measurement points falling into the gate in the second time segment. Next, each possible track is predicted, and a correlation gate is created centered on the prediction point. For the radar measurement point in the third time segment, if multiple points fall into the correlation gate, the points closest to the predicted point are selected to be associated with the existing trajectory. The possible trajectory will be cancelled if there is no effective radar measurement point falling in the correlation gate. The above

$$\left\{\hat{f}_{d,k}(t), 1 \le k \le K\right\} = \underset{\left\{\hat{f}_{d,k}(t), 1 \le k \le K\right\}}{\arg\min} \left\{ \sum_{k=1}^{K} \left\{ \begin{array}{l} -\int_{-\infty}^{\infty} \left| \mathrm{GST}\left[t, \hat{f}_{d,k}(t)\right] \right|^2 dt + \\ \int_{-\infty}^{\infty} \left[\mu_1 \cdot \hat{f}'_{d,k}(t)^2 + \mu_2 \cdot \hat{f}''_{d,k}(t)^2 \right] dt \end{array} \right\} \right\} \tag{25}$$

steps are repeated for subsequent time segments until a stable track is formed. For each time segment, the measurement points that do not fall into the correlation gate are used as the starting points of new trajectories, and track initiation is performed again.

Data association is the second step in multitarget tracking processing. This article selects the nearest neighbor algorithm to realize data association [38]. The following state and observation equations are established separately to achieve data association:

$$\mathbf{X}_{k,n} = \varphi\left(\mathbf{X}_{k,n-1}\right) + \mathbf{W}_k \tag{26}$$

$$\mathbf{Z}_{k,n} = \mathbf{H}\mathbf{X}_{k,n} + \mathbf{V}_k. \tag{27}$$

In the above equations, k denotes the scatterer index, n denotes the short time segment index, $\mathbf{X}$ represents the state vector, φ denotes a nonlinear function of the state vector $\mathbf{X}$, $\mathbf{Z}$ represents the measurement vector, $\mathbf{H}$ is the observation matrix, and $\mathbf{W}$ and $\mathbf{V}$ are the noise vectors in the state equation and the observation equation, respectively. The state vector, measurement vector, nonlinear function, and observation matrix can be expressed as

$$\mathbf{X}_{k,n} = \begin{bmatrix} f_{dc,k,n} & k_{r,k,n} \end{bmatrix}^T \tag{28}$$

$$\mathbf{Z}_{k,n} = f_{dc,k,n} \tag{29}$$

$$\varphi = \begin{bmatrix} \tan\left\{\arccos \dfrac{f_{dc,k,n} + T_{\text{seg}} \cdot k_{r,k,n}}{\frac{(k-1)T_{\text{seg}}}{\sqrt{\left(f_{dc,k,n}+T_{\text{seg}}\cdot k_{r,k,n}\right)^2+\left[(k-1)T_{\text{seg}}\right]^2}}}\right\} \end{bmatrix} \tag{30}$$

$$\mathbf{H} = \begin{bmatrix} 1 & 0 \end{bmatrix} \tag{31}$$

where $f_{dc,k,n}$ and $k_{r,k,n}$ denote the Doppler centroid frequency and frequency rate of the *k*th scatterer in the *n*th time segment, respectively. In the extended Kalman filtering, the prediction of the state is calculated by a nonlinear function, then the state transition matrix $\mathbf{F}$ in the Kalman filtering needs to be replaced by the Jacobian matrix of φ. After the approximate linearization of the nonlinear function is completed, the signal is filtered with the Kalman filtering framework [39]. The state transition matrix can be expressed as (32) shown at the bottom of this page.

Letting $\hat{\mathbf{X}}_{k,n}$ denote the estimated value of the state vector of the *k*th scatterer in the *n*th time segment, and letting $\hat{\mathbf{X}}^-_{k,n+1}$ denote the predicted value of the state vector of the *k*th scatterer in the $(n+1)$th time segment, obviously,

$$\hat{\mathbf{X}}^-_{k,n+1} = \mathbf{F}\hat{\mathbf{X}}_{k,n}. \tag{33}$$

Suppose there are K ridges in total, and the frequency of each ridge corresponding to the central moment of the $(n+1)$th time segment is $f_{d,k',n+1} 1 \le k' \le K$. In this article, the value of k' associated with k is selected according to the following principles:

$$k' = \arg\min_{k'} \left| f_{d,k',n+1} - \mathbf{H}\hat{\mathbf{X}}^-_{k,n+1} \right| 1 \le k' \le K. \tag{34}$$

The filtering process is the third step in multitarget tracking processing, and in this article, the Kalman filtering algorithm [40], [41], [42] is chosen to implement the filtering process. The state prediction equation is given in (33). In the prediction stage, the corresponding state covariance prediction equation is

$$\mathbf{P}^-_{k,n} = \mathbf{F}\mathbf{P}_{k,n-1}\mathbf{F}^T + \mathbf{Q} \tag{35}$$

where $\mathbf{P}$ denotes the state covariance matrix, the superscript - represents a predicted value, and $\mathbf{Q}$ denotes the state noise covariance matrix. The update phase involves the calculation of the Kalman gain matrix, the update of the state vector and the update of the state covariance matrix, which correspond to the following equations:

$$\mathbf{K}_{k,n} = \mathbf{P}^-_{k,n}\mathbf{H}^T\left(\mathbf{H}\mathbf{P}^-_{k,n}\mathbf{H}^T + \mathbf{R}\right)^{-1} \tag{36}$$

$$\hat{\mathbf{X}}_{k,n} = \hat{\mathbf{X}}^-_{k,n} + \mathbf{K}_{k,n}\left(\mathbf{Z}_{k,n} - \mathbf{H}\hat{\mathbf{X}}^-_{k,n}\right) \tag{37}$$

$$\mathbf{P}_{k,n} = \left(\mathbf{I} - \mathbf{K}_{k,n}\mathbf{H}\right)\mathbf{P}^-_{k,n}. \tag{38}$$

In the above equations, $\mathbf{K}_{k,n}$ is the Kalman gain matrix, $\mathbf{R}$ is the measurement noise covariance matrix, $\hat{\mathbf{X}}_{k,n}$ is the estimated value of the state vector of the *k*th scatterer in the *n*th time segment, $\hat{\mathbf{X}}^-_{k,n}$ is the prediction value of the state vector of the *k*th scatterer in the *n*th time segment, $\mathbf{Z}_{k,n}$ is the measurement vector corresponding to the *k*th scatterer in the *n*th time segment obtained after data association, $\mathbf{Z}_{k,n} - \mathbf{H}\hat{\mathbf{X}}^-_{k,n}$corresponds to the innovation matrix, and $\mathbf{I}$ is the identity matrix. Let N denote the number of total time segments; then, Kinstantaneous Doppler frequency signals $\{f_{d,k}(t), 1 \le k \le K\}$ corresponding

$$\mathbf{F} = \begin{bmatrix} \frac{\partial\varphi_1}{\partial f_{dc,k,n}} & \frac{\partial\varphi_1}{\partial k_{r,k,n}} \\ \frac{\partial\varphi_2}{\partial f_{dc,k,n}} & \frac{\partial\varphi_2}{\partial k_{r,k,n}} \end{bmatrix}$$

$$\frac{\partial\varphi_1}{\partial f_{dc,k,n}} = 1$$

$$\frac{\partial\varphi_1}{\partial k_{r,k,n}} = T_{\text{seg}}$$

$$\frac{\partial\varphi_2}{\partial f_{dc,k,n}} = \sec^2\left\{\arccos\frac{(k-1)\,T_{\text{seg}}}{\sqrt{\left(f_{dc,k,n}+T_{\text{seg}}\cdot k_{r,k,n}\right)^2+\left[(k-1)\,T_{seg}\right]^2}}\right\}\cdot\frac{(k-1)\,T_{\text{seg}}}{\left(f_{dc,k,n}+T_{\text{seg}}\cdot k_{r,k,n}\right)^2+\left[(k-1)\,T_{\text{seg}}\right]^2}$$

$$\frac{\partial\varphi_2}{\partial k_{r,k,n}} = \sec^2\left\{\arccos\frac{kT_{\text{seg}}}{\sqrt{\left(f_{dc,k,n}+T_{\text{seg}}\cdot k_{t,k,n}\right)^2+\left[(k-1)\,T_{seg}\right]^2}}\right\}\cdot\frac{(k-1)\,T_{\text{seg}}^2}{\left(f_{dc,k,n}+T_{\text{seg}}\cdot k_{r,k,n}\right)^2+\left[(k-1)\,T_{\text{seg}}\right]^2}. \tag{32}$$

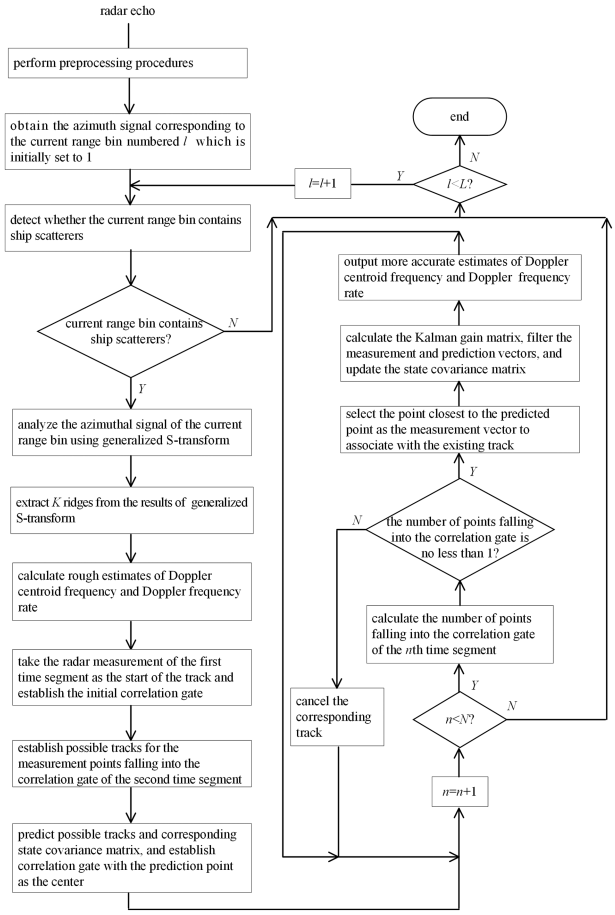

Fig. 5. Processing flow of the proposed algorithm.

to the current range bin whose index is l can be obtained after the above tracking process for K scatterers and N time segments.

E. Processing Flow of the Proposed Algorithm

Fig. 5 summarizes the processing flow of the algorithm proposed in this article. The radar echo signal is used as the input to the algorithm, which is preprocessed with range compression, envelope alignment, and translational phase compensation.

Let L denote the number of all range bins, l denote the index of the current range bin, and the initial value of l is set to 1. Then, the azimuth signal $s_l(t)$, which corresponds to the lth range bin, is detected by the constant false alarm rate algorithm described in Section III-B to determine whether there are ship scatterers in the current range bin. If there is no scatterer in the current range bin, then whether l is less than L is evaluated. If l is less than L, then the $(l+1)$th range bin is detected; otherwise, the processing flow ends.

If the lth range bin contains ship scatterers, then the algorithm combining the generalized S-transform with ridge extraction described in Section III-C is applied to coarsely estimate K time-frequency trajectories corresponding to $s_l(t)$.

After obtaining the rough instantaneous Doppler frequency trajectories, the azimuth time is divided into N time segments at intervals of T_{seg} with an empirical value of 0.1 s, and the estimated values of the Doppler centroid frequency and Doppler frequency rate corresponding to K ridges in each short time segment are calculated. Then, the track initiation, data association, and filtering of the time-frequency curves of each ship scatterer in the current range bin are performed using the linear micro-Doppler trajectory tracking algorithm, as described in Section III-D. The precise estimated values of each scatterer's Doppler centroid frequency and Doppler frequency rate corresponding to the lth range bin during the nth time segment are outputted. After the data of the nth time segment are processed, the data corresponding to the $(n+1)$th time segment are again processed until the data of all time segments are processed.

After the lth range bin is processed, the $(l+1)$th range bin is processed until all range bins are processed, and finally, precise estimation values of the instantaneous Doppler frequencies of all scatterers are outputted.

IV. Simulation and Real Data Processing Results

To illustrate the effectiveness of the algorithm proposed in this article, the processing of the simulated data and the processing of measured data acquired in turntable experiments were carried out. First, simulation experiments were conducted for two range bins containing two scatterers each. Simulated data were processed by the algorithm combining the generalized S-transform with ridge extraction, the algorithm in [23] and the proposed algorithm. The aim was to verify that the accuracy of the proposed algorithm is higher than those of the other two existing algorithms. Next, the real data of targets on a turntable were obtained using the SAR equipment installed on an intelligent car. Real data were also processed and compared using three algorithms to verify the highest accuracy and effectiveness in the actual environment with regard to the proposed algorithm.

A. Simulation Experiments and Results Analysis

The two scatterers' coordinates in the first range bin are set to [−26,12,0] and [80,12,0] in the $\xi\eta\zeta$ coordinate system, and the two scatterers' coordinates in the second range bin are set to [8,0,30] and [-80,3] in the $\xi\eta\zeta$ coordinate system. The synthetic aperture time is set to 10 s. Except for the scatterer coordinates and the synthetic aperture time, the settings of the remaining parameters are the same as the corresponding parameters in Table I.

Using the above simulation parameters, the algorithm combined the S-transform with ridge extraction, and the algorithm in [23] and the algorithm proposed in this article were performed. Fig. 6 shows the relevant processing results of the three algorithms, where Fig. 6(a) and (b) are the TFD maps corresponding to the first and the second range bins obtained by the generalized S-transform, respectively. After extracting the ridges of the results of the generalized S-transform, the instantaneous Doppler frequency estimation results of scatters in the first and second range bins can be obtained, as shown in Fig. 6(c) and (d). To facilitate the evaluation of the accuracy of the estimation results, Fig. 6(c) and (d) also show the true values of the instantaneous Doppler frequency of scatterers calculated according to the instantaneous distance variation between the radar and scatterers. The instantaneous Doppler frequency trajectories of the scatterers in Fig. 6(c) and (d) have relatively

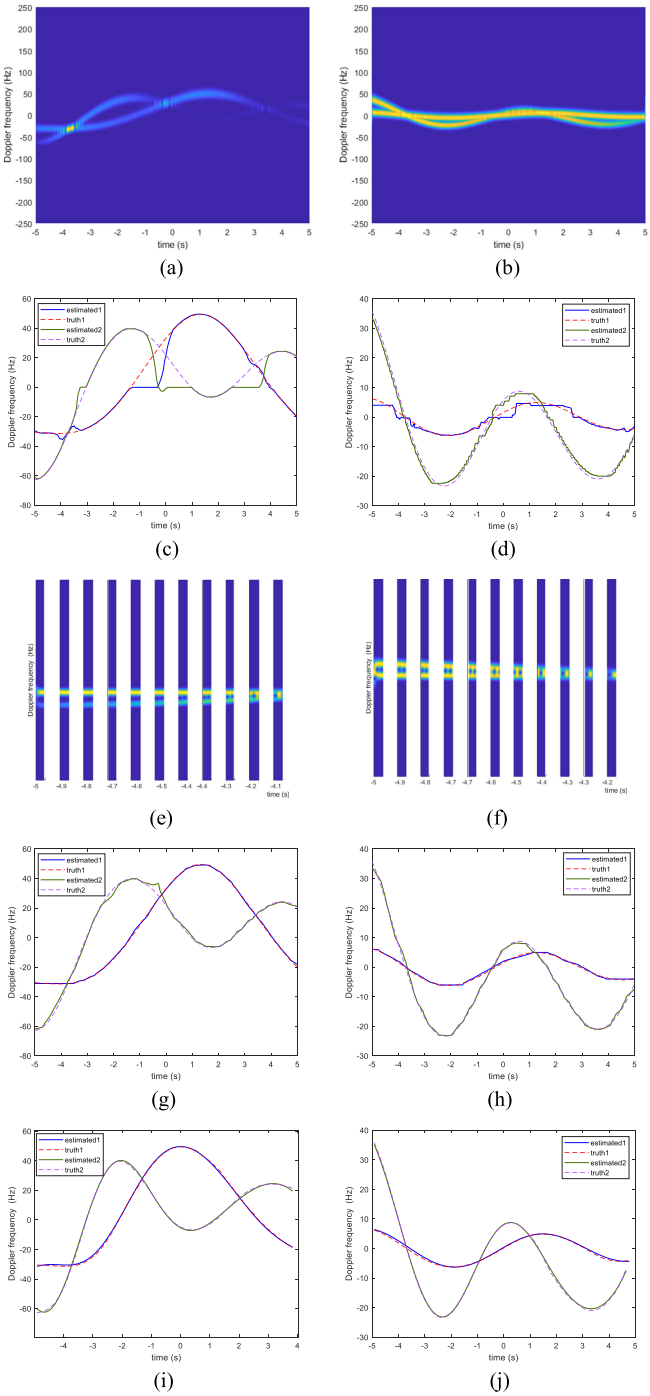

Fig. 6. Processing results in the simulation. (a) Time-frequency distribution of two scatterers in the first range bin generated by the generalized S-transform. (b) Time-frequency distribution of two scatterers in the second range bin generated by the generalized S-transform. (c) Instantaneous Doppler frequency curves of scatterers in the first range bin generated by the algorithm combining the generalized S-transform with ridge extraction. (d) Instantaneous Doppler frequency curves of the scatterers in the second range bin generated by the algorithm combining the generalized S-transform with ridge extraction. (e) Local information of Fig. 6(a). (f) Local information of Fig. 6(b). (g) Instantaneous Doppler frequency curves of the scatterers in the first range bin generated by the algorithm in [23]. (h) Instantaneous Doppler frequency curves of the scatterers in the second range bin generated by the algorithm in [23]. (i) Instantaneous Doppler frequency curves of the scatterers in the first range bin generated by the proposed algorithm. (j) Instantaneous Doppler frequency curves of the scatterer in the second range bin generated by the proposed algorithm.

TABLE II
MEAN SQUARE ERROR OF INSTANTANEOUS DOPPLER FREQUENCY ESTIMATED VALUES FOR THREE ALGORITHMS

Algorithm	Mean squared error of estimated values in the 1st range bin (Hz)	Mean squared error of estimated values in the 2nd range bin (Hz)
Generalized S-transform combined with the ridge extraction	8.09	12.19
[23]	1.44	0.66
Proposed	0.51	0.14

large errors at the intersection of the two trajectories. The mean square errors of the estimated values corresponding to Fig. 6(c) and (d) are approximately 8.09 and 12.19 Hz, respectively.

The length of the short time segment, T_{seg}, is set as 0.1 s in the simulation. With intervals of 0.1 s, Fig. 6(e) and (f) present the local information between -5 and -4.1 s in Fig. 6(a) and (b), respectively. Fig. 6(e) and (f) further verify that when the time segment is relatively short, the change in the instantaneous Doppler frequency of the scatterer approximately meets the characteristics of the linear frequency modulation signal.

Fig. 6(g) and (h) show the instantaneous Doppler frequency estimation results of scatterers in the first and second range bins obtained using the algorithm in [23], respectively. To qualitatively evaluate the accuracy of the estimated value, the true value curves of the instantaneous Doppler frequencies of scatterers are also shown in Fig. 6(g) and (h). Comparing the results in Fig. 6(c) and (d), it can be found that the algorithm in [23] achieves higher accuracy than that of the algorithm combining the generalized S-transform with ridge extraction. According to statistics, the mean square errors of the instantaneous Doppler frequency estimates corresponding to Fig. 6(g) and (h) are approximately 1.44 and 0.66 Hz, respectively.

Fig. 6(i) and (j) show the instantaneous Doppler frequency estimates of scatterers obtained using the proposed algorithm in the first and second range bins, respectively. As in the previous figures, the truth value curves of the instantaneous Doppler frequencies of scatterers are also shown in Fig. 6(i) and (j). It can be seen from Fig. 6(i) and (j) that good agreement is achieved between the estimated values and the true values of the instantaneous Doppler frequencies of scatterers. Statistically, the mean square errors of the instantaneous Doppler frequency estimates corresponding to Fig. 6(i) and (j) are approximately 0.51 and 0.14 Hz, respectively. It is clear that the proposed algorithm achieves higher estimation accuracy than those of the algorithm combining the generalized S-transform with ridge extraction and the algorithm in [23].

The mean squared errors of estimated values of the instantaneous Doppler frequency for the three algorithms are shown in Table II. It can be more clearly seen that the mean squared error of the proposed algorithm is smaller than that of the generalized S-transform combined with the ridge extraction algorithm, and that of the algorithm in [23]. Therefore, the estimation accuracy

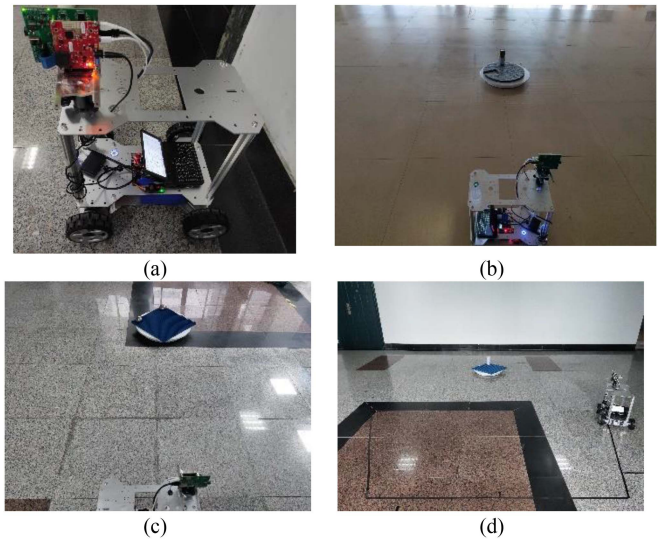

Fig. 7. Radar system and test scenario. (a) Photo of the radar system installed on an intelligent car. (b) Photo taken when the radar system is stationary to detect the metal can on the turntable. (c) Photo taken when the radar system is stationary to detect two metal balls on the turntable. (d) Photo taken when the radar system moves along the trapezoidal path to detect the metal can on the turntable.

of the instantaneous Doppler frequency using the proposed algorithm is the highest.

B. Real Data Validation and Results Analysis

A radar system platform consisting of an intelligent car and a turntable was built to collect real data to verify the effectiveness of the proposed algorithm in the actual environment. Fig. 7(a) shows a photo of the radar system installed on the intelligent car. Fig. 7(b) shows a picture taken when the radar system is stationary to detect a metal can on the turntable. Fig. 7(c) shows a photo taken when the radar system is stationary to detect two metal balls on the turntable. Fig. 7(d) shows a picture taken when the radar system moves along the trapezoidal path to detect a metal can on the turntable. It should be noted that it is difficult to collect the radar data of the ship and especially to obtain the motion attitude of the ship synchronously. Therefore, the rotation of the turntable and the movement of the smart car along a trapezoidal track are synthesized to simulate the movement of the ship to a certain extent. During the experiment, the motion parameters of the turntable and intelligent car can be accurately measured, so the true value of the Doppler frequency can be obtained.

The radar system consists of a TI IWR1443BOOST, DCA1000 capture card, an intelligent car equipped with STM32 as the main control, a speed control turntable, a Mini-PC, and TI mm wave studio software. The IWR1443BOOST board includes three transmit antenna arrays, four receive antenna arrays, and four receive channels. The IWR1443BOOST board transmits linear frequency modulation continuous waves and operates in the frequency range of 76–81 GHz and with a maximum bandwidth of 4 GHz. Radar transceiver parameters and data acquisition configuration are set through the TI mm wave studio software. After each experiment, the collected radar echo is

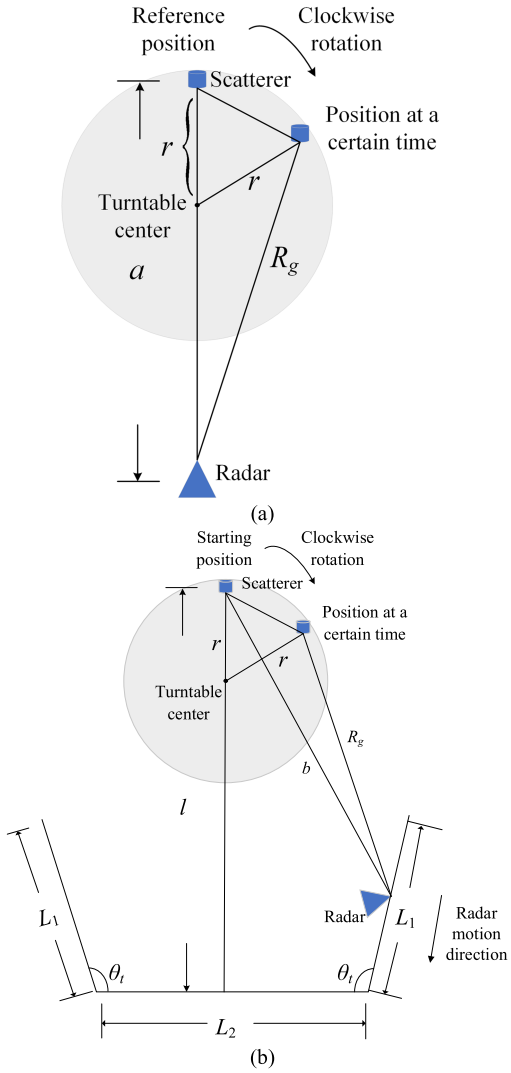

Fig. 8. Geometry of the turntable experiments. (a) Geometry of the case that the car is stationary. (b) Geometry of the case that the car is moving.

transferred to the workstation through a Gigabit Ethernet port, and a developed program is used for postprocessing on the workstation.

First, the intelligent car is stationary to collect the data of the metal can and two metal balls, respectively, during their clockwise rotations of a quarter circle on the turntable. Next, the intelligent car moves along a trapezoidal path to collect data of the metal can during its clockwise rotation of a quarter circle on the turntable. The travel time of the intelligent car along the trapezoidal path is designed to be equal to the period that the turntable rotates a quarter of a circle. Fig. 8(a) and (b) shows the geometric diagrams of the two kinds of tests, respectively. According to Fig. 8(a), the theoretical value of the instantaneous Doppler frequency when the intelligent car is stationary can be deduced as

$$R_g(t) = \sqrt{(a-r)^2 + r^2 + 2(a-r)\cdot r\cdot\cos\left[\omega\left(t-t_{\text{ref}}\right)\right]} \tag{39}$$

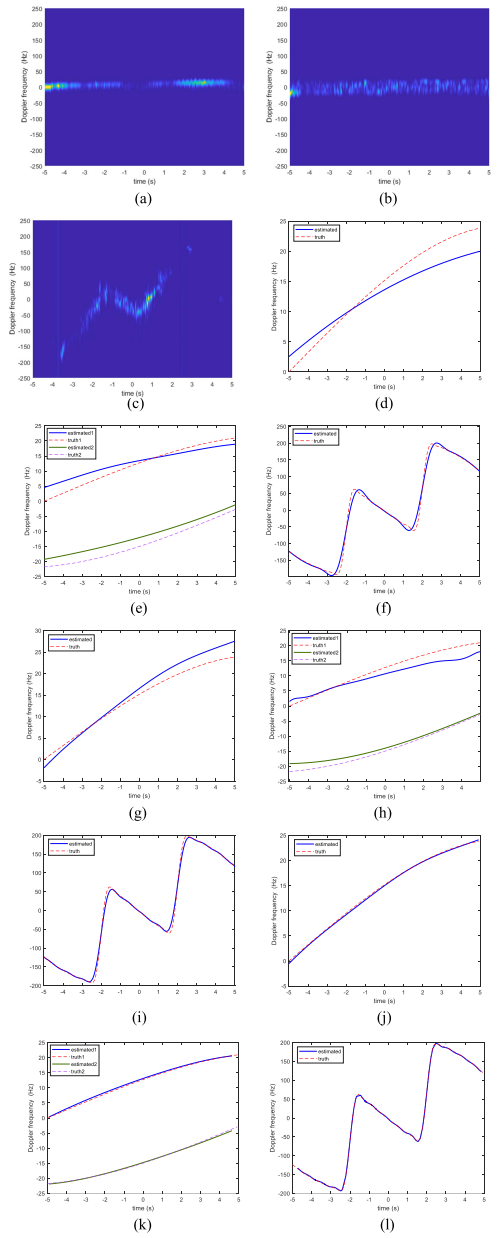

Fig. 9. Processing results of real data experiments. (a) Time-frequency distribution of the metal can when the car is stationary obtained using the generalized S-transform algorithm. (b) Time-frequency distributions of two metal balls when the car is stationary obtained using the generalized S-transform algorithm. (c) Time-frequency distribution of the metal can when the car is moving obtained using the generalized S-transform algorithm. (d) Instantaneous Doppler frequency curves of the metal can when the car is stationary estimated using the algorithm combining the generalized S-transform with ridge extraction. (e) Instantaneous Doppler frequency curves of two metal balls when the car is stationary estimated using the algorithm combining the generalized S-transform with ridge extraction. (f) Instantaneous Doppler frequency curves of the metal can when the car is moving estimated using the algorithm combining the generalized S-transform with ridge extraction. (g) Instantaneous Doppler frequency curves of the metal can when the car is stationary estimated using the algorithm in [23]. (h) Instantaneous Doppler frequency curves of two metal balls when the car is stationary estimated using the algorithm in [23]. (i) Instantaneous Doppler frequency curves of the metal can when the car is moving estimated using the algorithm in [23]. (j) Instantaneous Doppler frequency curves of the metal can when the car is stationary estimated using the proposed algorithm. (k) Instantaneous Doppler frequency curves of two metal balls when the car is stationary estimated using the proposed algorithm. (l) The instantaneous Doppler frequency curves of the metal can when the car is moving estimated using the proposed algorithm.

$$f_d(t) = -\frac{2}{\lambda}\frac{dR_g(t)}{dt} = \frac{2(a-r)\cdot r\cdot\omega\cdot\sin[\omega(t-t_{\text{ref}})]}{\lambda\sqrt{(a-r)^2+r^2+2(a-r)\cdot r\cdot\cos[\omega(t-t_{\text{ref}})]}} \tag{40}$$

where t denotes the time, a is the distance from the radar to the far end of the turntable along the radar line of sight, r is the radius of the turntable, ω is the rotational angular velocity of the turntable, t_{ref} is the moment when the target is at the farthest end of the turntable, λ is the wavelength, and $R_g(t)$ is the instantaneous distance between the scatterer and the radar.

According to Fig. 8(b), the formula to calculate the theoretical value of the instantaneous Doppler frequency when the car is moving and the turntable is rotating can be divided into four cases. When the car moves along the path whose length is L_1, the following expressions can be deduced as (41) and (42) shown at the bottom of the next page, where l represents the distance from the starting position of the target to the bottom edge of the trapezoidal path, L_1 and L_2 represent the lengths of the right and the middle line of the trapezoidal path, respectively, t denotes the time, t_{start} is the starting instant of the sampling period, θ_t represents the corner angle of the trapezoidal path, ω is the rotational angular velocity of the turntable, v represents the speed of the radar system, $b(t)$ is the instantaneous distance between the starting position of the target and the radar.

It is noted that the formula of the instantaneous Doppler frequency corresponding to (42) is too complex to be given. The true value of the instantaneous Doppler frequency when performing numerical calculation can be obtained by the difference operation on (42) and afterward multiplying a coefficient equal to $-2/\lambda$. Similarly, for the other three cases in the following, the explicit formulas of the instantaneous Doppler frequency are also not given.

When the car moves along the right half of the path whose length is L_2, the related theoretical value of the instantaneous Doppler frequency can be deduced as (43) and (44) shown at the bottom of the next page.

When the car moves along the left half of the path whose length is L_2, the related theoretical value of the instantaneous Doppler frequency can be deduced as (45) and (46) shown at the top of the next to next page.

When the car moves along the path whose length is L_3, the related theoretical value of the instantaneous Doppler frequency can be deduced as (47) and (48) shown at the top of the next to next page.

Table III shows the main parameters used in the turntable experiments. The truth values of the instantaneous Doppler frequencies were calculated based on the geometric relationship between the radar and the turntable, the turntable's angular speed, and other parameters.

After processing the range compression and performing translation compensation on the obtained echoes, the instantaneous Doppler frequencies were estimated using the algorithm combining the generalized S-transform with ridge extraction, the algorithm in [23], and the proposed algorithm. Fig. 9 shows

TABLE III
MAIN PARAMETERS USED IN THE TURNTABLE EXPERIMENTS

Parameter	Value	Parameter	Value
Carrier frequency	77 GHz	Bandwidth	3.7803 GHz
RPF	500 Hz	Accumulation time	10 s
ADC sampling frequency	17 MHz	Turntable's radius	30 cm
a in experiment that static car detects metal can	2.06 m	a in experiment that static car detects two balls	2.15 m
Turntable angular speed w in experiment that static car detects metal can	0.1571 rad/s	Turntable angular speed w in experiment that static car detects two balls	0.1428 rad/s
t_{ref} in experiment that static car detects metal can	-5 s	t_{ref} in experiment that static car detects two balls	Left ball: 5 s Right ball: -5 s
Turntable angular speed w in experiment that moving car detects metal can	0.1428 rad/s	radar system speed v in experiment that moving car detects metal can	0.5 m/s
l in experiment that moving car detects metal can	3.41 m	L_1 in experiment that moving car detects metal can	1.5 m
L_2 in experiment that moving car detects metal can	2 m	t_{start} in experiment that moving car detects metal can	-5 s
θ_t in experiment that moving car detects metal can	110°		

TABLE IV
MEAN SQUARE ERRORS OF INSTANTANEOUS DOPPLER FREQUENCY ESTIMATED VALUES IN TESTS USING INTELLIGENT CAR

Algorithm	Mean squared error of estimated values in metal can when car is stationary (Hz)	Mean squared error of estimated values in two metal balls when car is stationary (Hz)	Mean squared error of estimated values in metal can when car is moving (Hz)
Generalized S-transform combined with the ridge extraction	6.08	7.8	10.9
[23]	1.91	1.94	2.97
Proposed	0.49	0.17	1.0

the relevant processing results. Fig. 9(a)–(c) reveal the TFDs of the metal can and two metal balls when the car is stationary and the metal can as the car moves along the trapezoidal path obtained using the generalized S-transform algorithm, respectively. Fig. 9(d)–(f) plot the instantaneous Doppler frequency estimation results of the metal can and two metal balls when the car is stationary and the metal can as the car moves along the trapezoidal path obtained using the algorithm combining the generalized S-transform with ridge extraction, respectively. Truth value curves are also displayed in Fig. 9(d)–(f) and subsequent subfigures in Fig. 9. Statistically, the mean square errors of the instantaneous Doppler frequency estimation error are approximately 6.08, 7.8, and 10.9 Hz in Fig. 9(d)–(f), respectively. Fig. 9(g)–(i) depict the results of the instantaneous Doppler frequency estimation for the metal can and two metal balls when the car is stationary and the metal can as the car moves along the trapezoidal path obtained using the algorithm in [23], respectively. The mean square errors of the instantaneous Doppler frequency estimation error are approximately 1.91, 1.94, and 2.97 Hz in the three pictures, respectively. Fig. 9(j)–(l) present the instantaneous Doppler frequency estimation results of the metal can and two metal balls when the car is stationary and the metal can as the car moves along the trapezoidal path obtained using the proposed algorithm. The mean square errors of the instantaneous Doppler frequency estimation error are approximately 0.49, 0.17, and 1.0 Hz in the three pictures. Table IV shows the mean squared error of the instantaneous Doppler frequency estimation error for the three algorithms, respectively. By comparison, the proposed algorithm achieves the highest estimation accuracy. Therefore, the experimental results verify

$$b(t)=\sqrt{\left[l-\left[L_1-v\left(t-t_{\text{start}}\right)\right]\sin\theta_t\right]^2+\left[\frac{L_2}{2}-\left[L_1-v\left(t-t_{\text{start}}\right)\right]\cos\theta_t\right]^2} \tag{41}$$

$$R_g(t)=\sqrt{\begin{array}{r} b^2(t)+2r^2-2r^2\cos\left[\omega\left(t-t_{\text{start}}\right)\right]-2b(t)\sqrt{2r^2-2r^2\cos\left[\omega\left(t-t_{\text{start}}\right)\right]}\cdot \\ \cos\left\{\frac{\pi-\omega\left(t-t_{\text{start}}\right)}{2}-\arctan\left\{\frac{\frac{L_2}{2}-\left[L_1-v\left(t-t_{\text{start}}\right)\right]\cos\theta_t}{l-\left[L_1-v\left(t-t_{\text{start}}\right)\right]\sin\theta_t}\right\}\right\}\end{array}} \tag{42}$$

$$b(t)=\sqrt{l^2+\left\{\frac{L_2}{2}-v\left[t-\left(t_{\text{start}}+\frac{L_1}{v}\right)\right]\right\}^2} \tag{43}$$

$$R_g(t)=\sqrt{\begin{array}{r} b^2(t)+2r^2-2r^2\cos\left[\omega\left(t-t_{\text{start}}\right)\right]-2b(t)\sqrt{2r^2-2r^2\cos\left[\omega\left(t-t_{\text{start}}\right)\right]}\cdot \\ \cos\left\{\frac{\pi-\omega\left(t-t_{\text{start}}\right)}{2}-\arctan\left\{\frac{\frac{L_2}{2}-v\left[t-\left(t_{\text{start}}+\frac{L_1}{v}\right)\right]}{l}\right\}\right\}.\end{array}} \tag{44}$$

$$b(t)=\sqrt{l^2+v^2\left[t-\left(t_{\text{start}}+\frac{L_1+L_2/2}{v}\right)\right]^2} \tag{45}$$

$$R_g(t)=\sqrt{\begin{array}{c}b^2(t)+2r^2-2r^2\cos\left[\omega\left(t-t_{\text{start}}\right)\right]-2b(t)\sqrt{2r^2-2r^2\cos\left[\omega\left(t-t_{\text{start}}\right)\right]}\cdot\\ \cos\left\{\frac{\pi-\omega\left(t-t_{\text{start}}\right)}{2}+\arctan\left\{\frac{v\left[t-\left(t_{\text{start}}+\frac{L_1+L_2/2}{v}\right)\right]}{l}\right\}\right\}.\end{array}} \tag{46}$$

$$b(t)=\sqrt{\begin{array}{l}\left\{l-v\left[t-\left(t_{\text{start}}+\frac{L_1+L_2}{v}\right)\right]\sin\theta_t\right\}^2+\\ \left\{\frac{L_2}{2}-v\left[t-\left(t_{\text{start}}+\frac{L_1+L_2}{v}\right)\right]\cos\theta_t\right\}^2\end{array}} \tag{47}$$

$$R_g(t)=\sqrt{\begin{array}{c}b^2(t)+2r^2-2r^2\cos\left[\omega\left(t-t_{\text{start}}\right)\right]-2b(t)\sqrt{2r^2-2r^2\cos\left[\omega\left(t-t_{\text{start}}\right)\right]}\cdot\\ \cos\left\{\frac{\pi-\omega\left(t-t_{\text{start}}\right)}{2}+\arctan\left\{\frac{\frac{L_2}{2}-v\left[t-\left(t_{\text{start}}+\frac{L_1+L_2}{v}\right)\right]\cos\theta_t}{l-v\left[t-\left(t_{\text{start}}+\frac{L_1+L_2}{v}\right)\right]\sin\theta_t}\right\}\right\}.\end{array}} \tag{48}$$

the highest accuracy and effectiveness of the proposed algorithm in an actual environment.

V. Conclusion

Precise extraction of the 3-DOF micromotion features caused by a ship's rotations in the three axes of roll, pitch, and yaw are essential for improving the microwave imaging quality of ships and realizing the ship's 3-D imaging. However, when the accumulation time is relatively long (for example, more than 10 s), the extraction accuracy of existing algorithms is low. This article proposes a new algorithm based on linear Doppler trajectory tracking to precisely extract 3-DOF micromotion features under long accumulation times.

The algorithm performs range compression and translation compensation on the echo and then detects range bins containing the ship scatterers. Then, an algorithm combining the generalized S-transform with ridge extraction is used to achieve a rough estimation of the time-frequency trajectories of ship scatterers, and the whole accumulation time is divided into many short time segments. After that, the Doppler centroid frequency and Doppler frequency rate of each short time segment are estimated. Finally, to achieve accurate estimates of instantaneous Doppler frequencies over a long time, multitarget tracking-related methods, such as nearest neighbor data association and extended Kalman filtering are used to correlate and filter the estimated values of the instantaneous Doppler frequencies belonging to the same scatterer in adjacent short time segments. The core idea of the proposed algorithm is to approximate a curve with a broken line composed of multiple short lines, which takes advantage of the characteristic that the instantaneous Doppler frequency of a scatterer caused by the 3-D rotations of a ship behaves as a linear frequency modulation signal over a short time. Several experiments were carried out in terms of simulation and real data processing. The instantaneous Doppler frequency estimation results of the proposed algorithm are compared with those of the algorithm combining the generalized S-transform with ridge extraction and the algorithm in [23], and the proposed algorithm achieves the highest accuracy.

After extracting the 3-DOF micromotion feature information with high accuracy, the future work is to construct the relationship between the micromotion features, the 3-D coordinates of ship scatterers, and the three-axis rotation parameters of a ship. Besides, approaches to estimate three-axis rotation parameters of a ship and to inverse 3-D coordinates of ship scatterers are to be developed. Thus, the 3-D SAR image of a moving ship can be generated.

Acknowledgment

The authors would like to thank the anonymous reviewers for their valuable comments and suggestions, which helped to substantially improve the quality of this article.

References

[1] C. Chen, C. He, C. Hu, H. Pei, and L. C. Jiao, "A deep neural network based on an attention mechanism for SAR ship detection in multiscale and complex scenarios," *IEEE Access*, vol. 7, pp. 104848–104863, 2019.

[2] X. Zhang et al., "Multitask learning for ship detection from synthetic aperture radar images," *IEEE J. Sel. Topics Appl. Earth Observ. Remote Sens.*, vol. 14, pp. 8048–8062, 2021.

[3] Z. Liu, Y. Jiang, Y. Wang, and Y. Du, "Radar imaging of nonstationary rotating ship target with GEO-shipborne bistatic configuration," *IEEE Sensors J.*, vol. 19, no. 13, pp. 5213–5218, Jul. 2019.

[4] N. Li, Q. Shen, L. Wang, Q. Wang, Z. Guo, and J. Zhao, "Optimal time selection for ISAR imaging of ship targets based on time-frequency analysis of multiple scatterers," *IEEE Geosci. Remote Sens. Lett.*, vol. 19, 2022, Art no. 4017505.

[5] Y. Wang and X. Chen, "3-D InISAR imaging of the ship target based on joint cross s-method algorithm," *IEEE Geosci. Remote Sens. Lett.*, vol. 16, no. 7, pp. 1080–1084, Jul. 2019.

[6] J. Ai et al., "Robust CFAR ship detector based on bilateral-trimmed-statistics of complex ocean scenes in SAR imagery: A closed-form solution," *IEEE Trans. Aerosp. Electron. Syst.*, vol. 57, no. 3, pp. 1872–1890, Jun. 2021.

[7] J. Ai, R. Tian, Q. Luo, J. Jin, and B. Tang, "Multi-scale rotation-invariant haar-like feature integrated CNN-based ship detection algorithm of multiple-target environment in SAR imagery," *IEEE Trans. Geosci. Remote Sens.*, vol. 57, no. 12, pp. 10070–10087, Dec. 2019.

[8] J. He, Y. Wang, and H. Liu, "Ship classification in medium-resolution SAR images via densely connected triplet CNNs integrating fisher discrimination regularized metric learning," *IEEE Trans. Geosci. Remote Sens.*, vol. 59, no. 4, pp. 3022–3039, Apr. 2021.
[9] Y. Sun, Z. Wang, X. Sun, and K. Fu, "SPAN: Strong scattering point aware network for ship detection and classification in large-scale SAR imagery," *IEEE J. Sel. Topics Appl. Earth Observ. Remote Sens.*, vol. 15, pp. 1188–1204, 2022.
[10] A. Hanif, M. Muaz, A. Hasan, and M. Adeel, "Micro-doppler based target recognition with radars: A review," *IEEE Sensors J.*, vol. 22, no. 4, pp. 2948–2961, Feb. 2022.
[11] X. Xu, C. Feng, and S. He, "A method for the micro-motion signal separation and micro-Doppler extraction for the space precession target," *IEEE Access*, vol. 8, pp. 130392–130404, 2020.
[12] J. Zhong and Y. Huang, "Time-frequency representation based on an adaptive short-time Fourier transform," *IEEE Trans. Signal Process.*, vol. 58, no. 10, pp. 5118–5128, Oct. 2010.
[13] S. Wang, X. Chen, C. Tong, and Z. Zhao, "Matching synchrosqueezing wavelet transform and application to aeroengine vibration monitoring," *IEEE Trans. Instrum. Meas.*, vol. 66, no. 2, pp. 360–372, Feb. 2017.
[14] R. G. Stockwell, L. Mansinha, and R. P. Lowe, "Localization of the complex spectrum: The s transform," *IEEE Trans. Signal Process.*, vol. 44, no. 4, pp. 998–1001, Apr. 1996.
[15] A. Y. Erdogan, T. O. Gulum, L. Durak-Ata, T. Yildirim, and P. E. Pace, "FMCW signal detection and parameter extraction by cross Wigner–Hough transform," *IEEE Trans. Aerosp. Electron. Syst.*, vol. 53, no. 1, pp. 334–344, Feb. 2017.
[16] X. Xiong, H. Liu, Z. M. Deng, M. Z. Fu, W. Qi, and Y. J. Zhang, "Micro-doppler ambiguity resolution with variable shrinkage ratio based on time-delayed cross correlation processing for wideband radar," *IEEE Trans. Geosci. Remote Sens.*, vol. 57, no. 4, pp. 1906–1917, Apr. 2019.
[17] Y. Ding, Y. Sun, G. Huang, R. Liu, X. Yu, and X. Xu, "Human target localization using Doppler through-wall radar based on micro-Doppler frequency estimation," *IEEE Sensors J.*, vol. 20, no. 15, pp. 8778–8788, Aug. 2020.
[18] P. Suresh, T. Thayaparan, T. Obulesu, and K. Venkataramaniah, "Extracting micro-Doppler radar signatures from rotating targets using Fourier–Bessel transform and time–frequency analysis," *IEEE Trans. Geosci. Remote Sens.*, vol. 52, no. 6, pp. 3204–3210, Jun. 2014.
[19] Y. Abdoush, G. Pojani, and G. E. Corazza, "Adaptive instantaneous frequency estimation of multicomponent signals based on linear time-frequency transforms," *IEEE Trans. Signal Process.*, vol. 67, no. 12, pp. 3100–3112, Jun. 2019.
[20] X. Fang and G. Xiao, "Rotor blades micro-Doppler feature analysis and extraction of small unmanned rotorcraft," *IEEE Sensors J.*, vol. 21, no. 3, pp. 3592–3601, Feb. 2021.
[21] X. Bai, F. Zhou, M. Xing, and Z. Bao, "High resolution ISAR imaging of targets with rotating parts," *IEEE Trans. Aerosp. Electron. Syst.*, vol. 47, no. 4, pp. 2530–2543, Oct. 2011.
[22] B. Peng, X. Wei, B. Deng, H. Chen, Z. Liu, and X. Li, "A sinusoidal frequency modulation Fourier transform for radar-based vehicle vibration estimation," *IEEE Trans. Instrum. Meas.*, vol. 63, no. 9, pp. 2188–2199, Sep. 2014.
[23] P. Zhou, X. Zhang, Y. Dai, W. Sun, and Y. Wan, "Time window selection algorithm for ISAR ship imaging based on instantaneous doppler frequency estimations of multiple scatterers," *IEEE J. Sel. Topics Appl. Earth Observ. Remote Sens.*, vol. 12, no. 10, pp. 3799–3812, Oct. 2019.
[24] Y. Wang and X. Chen, "3-D interferometric inverse synthetic aperture radar imaging of ship target with complex motion," *IEEE Trans. Geosci. Remote Sens.*, vol. 56, no. 7, pp. 3693–3708, Jul. 2018.
[25] P. Liu and Y. Q. Jin, "A study of ship rotation effects on SAR image," *IEEE Trans. Geosci. Remote Sens.*, vol. 55, no. 6, pp. 3132–3144, Jun. 2017.
[26] X. Xu, F. Su, J. Gao, and X. Jin, "High-squint SAR imaging of maritime ship targets," *IEEE Trans. Geosci. Remote Sens.*, vol. 60, 2022, Art no. 5200716.
[27] P. Zhou, M. Martorella, X. Zhang, Y. Dai, W. Sun, and Y. Wan, "Circular scan ISAR mode super-resolution imaging of ships based on a combination of data extrapolation and compressed sensing," *IEEE Sensors J.*, vol. 19, no. 16, pp. 6883–6894, Aug. 2019.
[28] D. R. Wehner, *High-Resolution Radar*. Boston, MA, USA: Artech House, 1995, pp. 408–411.
[29] N. Liu, J. Gao, B. Zheng, F. Li, and Q. Wang, "Time–frequency analysis of seismic data using a three parameters S transform," *IEEE Geosci. Remote Sens. Lett.*, vol. 15, no. 1, pp. 142–146, Jan. 2018.
[30] B. Wang and W. Lu, "An efficient amplitude-preserving generalized S transform and its application in seismic data attenuation compensation," *IEEE Trans. Geosci. Remote Sens.*, vol. 56, no. 2, pp. 859–866, Feb. 2018.
[31] G. Yu, M. Yu, and C. Xu, "Synchroextracting transform," *IEEE Trans. Ind. Electron.*, vol. 64, no. 10, pp. 8042–8054, Oct. 2017.
[32] R. A. Carmona, W. L. Hwang, and B. Torresani, "Characterization of signals by the ridges of their wavelet transforms," *IEEE Trans. Signal Process.*, vol. 45, no. 10, pp. 2586–2590, Oct. 1997.
[33] G. Yu, Z. Wang, and P. Zhao, "Multisynchrosqueezing transform," *IEEE Trans. Ind. Electron.*, vol. 66, no. 7, pp. 5441–5455, Jul. 2019.
[34] M. L. Jayaramu, H. N. Suresh, M. S. Bhaskar, D. Almakhles, S. Padmanaban, and U. Subramaniam, "Real-time implementation of extended Kalman filter observer with improved speed estimation for sensorless control," *IEEE Access*, vol. 9, pp. 50452–50465, 2021.
[35] G. Y. Kulikov and M. V. Kulikov, "The accurate continuous-discrete extended Kalman filter for radar tracking," *IEEE Trans. Signal Process.*, vol. 64, no. 4, pp. 948–958, Feb. 2016.
[36] A. Sinha, Z. Ding, T. Kirubarajan, and M. Farooq, "Track quality based multitarget tracking approach for global nearest-neighbor association," *IEEE Trans. Aerosp. Electron. Syst.*, vol. 48, no. 2, pp. 1179–1191, Apr. 2012.
[37] Z. Hu, H. Leung, and M. Blanchette, "Statistical performance analysis of track initiation technique," *IEEE Trans. Signal Process.*, vol. 45, no. 2, pp. 445–456, Feb. 1997.
[38] X. R. Li and Y. Bar-Shalom, "Tracking in clutter with nearest neighbor filters: Analysis and performance," *IEEE Trans. Aerosp. Electron. Syst.*, vol. 32, no. 3, pp. 995–1010, Jul. 1996.
[39] X. Liu, Z. Ren, H. Lyu, Z. Jiang, P. Ren, and B. Chen, "Linear and nonlinear regression-based maximum correntropy extended Kalman filtering," *IEEE Trans. Syst., Man, Cybern. Syst.*, vol. 51, no. 5, pp. 3093–3102, May 2021.
[40] D. Reid, "An algorithm for tracking multiple targets," *IEEE Trans. Autom. Control*, vol. 24, no. 6, pp. 843–854, Dec. 1979.
[41] S. Chen and C. Shao, "Efficient online tracking-by-detection with Kalman filter," *IEEE Access*, vol. 9, pp. 147570–147578, 2021.
[42] R. A. Singer, "Estimating optimal tracking filter performance for manned maneuvering targets," *IEEE Trans. Aerosp. Electron. Syst.*, vol. AES-6, no. 4, pp. 473–483, Jul. 1970.

Peng Zhou (Member, IEEE) received the B.S. degree in electronic engineering and the M.S. degree in automation control engineering from the China University of Petroleum, Dongying, China, in 1997 and 2000, respectively, and the Ph.D. degree in signal and information processing from the University of Electronic Science and Technology of China, Chengdu, China, in 2008.

He is an Associate Professor with the College of Oceanography and Space Informatics, China University of Petroleum, Qingdao, China. From December 2017 to November 2018, he worked as a Visiting Researcher with the Department of Information Engineering, University of Pisa, Pisa, Italy. His research interests include SAR imaging, ISAR imaging, and especially topics related to the radar imaging of ships.

Chuwen Cao received the B.S. degree in communication engineering from Ludong University, Yantai, China, in 2020. She is currently working toward the M.S. degree in information and communication engineering with the College of Oceanography and Space Informatics, China University of Petroleum, Qingdao, China.

Her research interest is microwave imaging of ships.

Yuru Li received the B.S. degree in electronic information engineering from the Shandong University of Technology, Zibo, China, in 2019. She is currently working toward the M.S. degree in electronic and information with the College of Oceanography and Space Informatics, China University of Petroleum, Qingdao, China.

Her research interest is the construction of millimeter wave radar imaging systems.

Xi Zhang received the B.S. degree in information systems from the Qingdao University of Science and Technology, Qingdao, China, in 2005, the M.S. degree in signal and information processing and the Ph.D. degree in computer science from the Ocean University of China, Qingdao, China, in 2008 and 2011, respectively.

He is currently a Researcher with the First Institute of Oceanography, Ministry of Natural Resources of the People's Republic of China, Qingdao, China. His research interests include the remote sensing of oceans and SAR imaging.

Zhenhua Zhang received the Ph.D. degree in signal processing from the Xidian University, Xi'an, China, in 2007.

He is currently a Researcher with Beijing Research Institute of Telemetry, Beijing, China. His research interests include SAR imaging and radar signal processing.

Jie Zhang received the B.S. and M.S. degrees in mathematics from Inner Mongolia University, Huhhot, China, in 1984 and 1987, respectively, and the Ph.D. degree in applied mathematics from Tsinghua University, Beijing, China, in 1993.

He is the Dean of the College of Oceanography and Space Informatics, China University of Petroleum, Qingdao, China. His research interests include SAR retrieval of ocean dynamics processes and SAR detection of marine targets, ocean hyperspectral remote sensing, ocean detection techniques utilizing high-frequency surface wave radar, and the integration of marine remote sensing application systems.